






One-step synthesis of single-site vanadium substitution in 1T-WS₂ monolayers for enhanced hydrogen evolution catalysis

Ali Han^{1,2,9}, Xiaofeng Zhou^{1,3,9}, Xijun Wang ^{4,9}, Sheng Liu⁵, Qihua Xiong ^{5,6}, Qinghua Zhang⁷, Lin Gu⁷, Zechao Zhuang², Wenjing Zhang⁸, Fanxing Li ⁴, Dingsheng Wang ^{2✉}, Lain-Jong Li ^{1✉} & Yadong Li²

Metallic tungsten disulfide (WS₂) monolayers have been demonstrated as promising electrocatalysts for hydrogen evolution reaction (HER) induced by the high intrinsic conductivity, however, the key challenges to maximize the catalytic activity are achieving the metallic WS₂ with high concentration and increasing the density of the active sites. In this work, single-atom-V catalysts (V SACs) substitutions in 1T-WS₂ monolayers (91% phase purity) are fabricated to significantly enhance the HER performance via a one-step chemical vapor deposition strategy. Atomic-resolution scanning transmission electron microscopy (STEM) imaging together with Raman spectroscopy confirm the atomic dispersion of V species on the 1T-WS₂ monolayers instead of energetically favorable 2H-WS₂ monolayers. The growth mechanism of V SACs@1T-WS₂ monolayers is experimentally and theoretically demonstrated. Density functional theory (DFT) calculations demonstrate that the activated V-atom sites play vital important role in enhancing the HER activity. In this work, it opens a novel path to directly synthesize atomically dispersed single-metal catalysts on metastable materials as efficient and robust electrocatalysts.

¹Physical Sciences and Engineering Division, King Abdullah University of Science and Technology, Thuwal 23955-6900, Kingdom of Saudi Arabia. ²Department of Chemistry, Tsinghua University, Beijing 100084, China. ³Shenzhen Chang Long Technology Co., Ltd, Shenzhen 518117, China. ⁴Department of Chemical and Biomolecular Engineering, North Carolina State University, Raleigh, NC 27606, USA. ⁵Division of Physics and Applied Physics, School of Physical and Mathematical Sciences, Nanyang Technological University, Nanyang Ave, Singapore 637371, Singapore. ⁶State Key Laboratory of Low-Dimensional Quantum Physics and Department of Physics, Tsinghua University, Beijing 100084, China. ⁷Beijing National Laboratory for Condensed Matter Physics, Institute of Physics, Chinese Academy of Sciences, Beijing 100190, China. ⁸SZU-NUS Collaborative Innovation Center for Optoelectronic Science & Technology, Key Laboratory of Optoelectronic Devices and Systems of Ministry of Education and Guangdong Province, College of Optoelectronic Engineering, Shenzhen University, Shenzhen 518060, China. ⁹These authors contributed equally: Ali Han, Xiaofeng Zhou, Xijun Wang. ✉email: wangdingsheng@mail.tsinghua.edu.cn; lance.li@kaust.edu.sa

Hydrogen fuel generation from water splitting is one of the most promising ways to replace conventional fossil fuels and solve the energy crisis^{1,2}. Recently, various strategies have been developed to realize the highly efficient catalysts for hydrogen evolution reaction (HER), including semiconductor-based photocatalytic HER (polymer $g\text{-C}_3\text{N}_4$ ³, Ag/semiconductor⁴, etc.), photoelectrochemically catalytic HER⁵, and metal-based electrocatalytic HER (metal sulfides^{1,6,7}, metal carbides^{8,9}, etc.). Commercially, noble metals from the Pt group are utilized to reduce the overpotential of HER and boost the kinetics with unrivaled activities, however, they usually suffer from scarcity, high-cost, and long-term instability. Hence, it is highly desirable to explore robust and efficient HER alternative catalysts with earth-abundant elements to realize the hydrogen economy.

Transition metal dichalcogenides (TMDs) from Group VI elements have recently kindled tremendous investigation as efficient Pt substitutes for HER catalysis because of the catalytically active S atoms on edge sites¹⁰. Unfortunately, the high proportion of inactive basal plane of MX_2 ($M = \text{Mo}$ or W , $X = \text{S}$ or Se) significantly limits the catalytic performance because of the low electronic transfer capability, leading to the sluggish electrocatalytic kinetics¹. Two key factors are worthy of being considered to maximize HER activity. One is to increase the metallic phase proportion of MX_2 , thus improving the intrinsic conductivity of MX_2 and boosting HER activity^{2,6,11}. However, it is still challenging to directly synthesize a highly pure metallic phase, especially for 1T- WS_2 , owing to the highest formation energy of 1T- WS_2 (0.89 eV per formula) among all the polymorphs of MX_2 (Supplementary Fig. 1)¹². Recently, the phase-engineered syntheses of metallic MX_2 from the 2H phase have been widely developed via wet-chemistry or exfoliated methods, however, the as-produced metallic MX_2 domains were usually found with 1T(1T')/2H mixed-phase and unstable after long-time air-exposure^{1,2,6,7,13–22}. The other important factor is increasing the density of active sites of MX_2 . The field of single atomic catalysts (SACs) comprising isolated metal atoms on the varied supports gives new opportunities for the development of MX_2 with increased active sites due to the high atom utilization of SACs^{23–25}. However, to the best of

our knowledge, the reports on the direct one-step vapor-phase synthesis of SACs on the highly pure metallic MX_2 have not been explored.

Here, we show highly dispersed single vanadium atoms on the 1T- WS_2 monolayers (denoted as V SACs@1T- WS_2), which are synthesized through a one-step chemical vapor deposition (CVD) via controlling the introduction of VCl_3 . By using VCl_3 as the co-precursor, the metallic tungsten disulfide (WS_2) monolayers show an ultrahigh 1T concentration of 91%, which is the highest 1T ratio achieved by CVD so far (Supplementary Table 1). Remarkably, the V SACs@1T- WS_2 monolayers show superior HER activity comparable to their 2H counterparts, with a low Tafel slope of 61 mV/dec and high turnover frequency (TOF) of 3.01 s^{-1} at 100 mV, and a remarkable long-term catalytic stability. We also demonstrate that the highly active single-atom V sites play a vital role in enhancing the HER activity of intrinsic 1T- WS_2 monolayers.

Results

Characterization of V SACs@1T- WS_2 monolayers. Figure 1 shows the scheme for the growth of V SACs@1T- WS_2 monolayers using WO_3 , sulphur, and VCl_3 as the co-precursors. For comparison, 2H- WS_2 monolayers were prepared without using the VCl_3 co-precursor at the same condition and the growth process has been reported elsewhere^{26–33}. Strikingly, a black film of V_2O_5 (Fig. 2a and Supplementary Fig. 2) was observed on the sapphire surface during the V SACs@1T- WS_2 monolayers growth, while no V_2O_5 film appeared for the 2H- WS_2 monolayers growth. The optical micrographs of fresh sapphire and V_2O_5 film were also provided here for comparison, as seen in Supplementary Fig. 3a, b. In sharp contrast to the triangular morphology of 2H- WS_2 (Fig. 2b), the V SACs@1T- WS_2 monolayers show a uniformly circular morphology with a lateral size of $30 \mu\text{m}$ (Fig. 2b and Supplementary Fig. 3c).

The atomic structure of V SACs@1T- WS_2 monolayers was investigated by the aberration-corrected STEM, as provided in Fig. 2c, d, showing that the evident Z-contrast intensity sites are

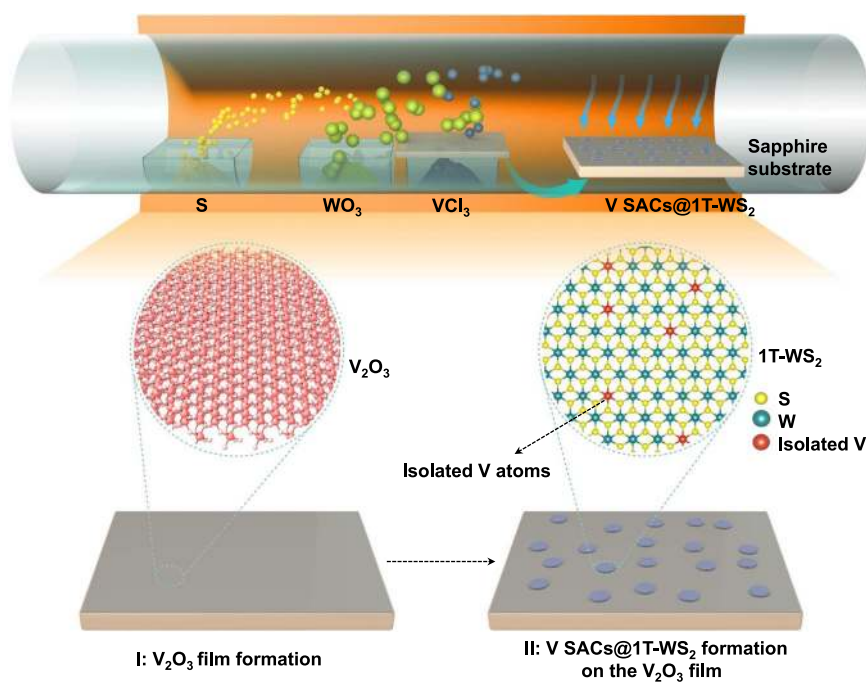


Fig. 1 Schematic illustration of the synthetic process for V SACs@1T- WS_2 monolayers. I V_2O_5 formation in the early growth stage. **II** V SACs@1T- WS_2 monolayers formed on the V_2O_5 film.

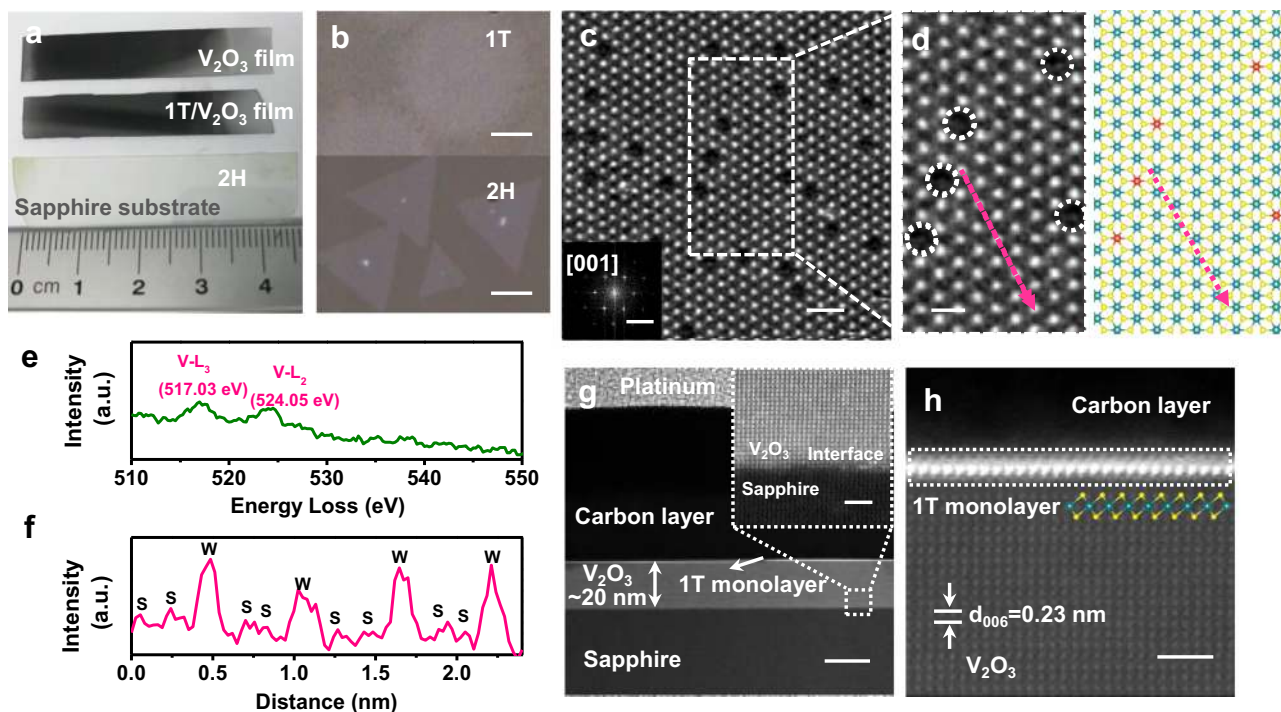


Fig. 2 Characterization of V SACs@1T-WS₂ monolayers. **a** Pictures of different materials formed on the sapphire substrates. Up: V₂O₅ film; Middle: V SACs@1T-WS₂/V₂O₃ film; down: 2H-WS₂. **b** Optical micrographs of as-grown V SACs@1T-WS₂ (up) and 2H-WS₂ (down) grown by CVD. **c** High-resolution HAADF-STEM image for the V SACs@1T-WS₂. Inset: the corresponding fast Fourier transform (FFT) of **(c)**. **d** Left: zoom-in high-resolution STEM image for the V SACs@1T-WS₂ indicated by **(c)**. Right: the schematic model of V SACs@1T-WS₂. The blue spheres, yellow spheres, and red spheres represent the W atoms, S atoms, and V atoms, respectively. **e** EELS spectrum of vanadium element in the V SACs@1T-WS₂ monolayer. **f** Intensity profiles of the pink dashed arrow indicated by Fig. 1d. **g** Low-resolution cross-section HAADF-STEM image of V SACs@1T-WS₂/V₂O₃ film on the sapphire substrate. Inset: the interface between V₂O₃ and sapphire substrate. **h** High-resolution HAADF-STEM image of V SACs@1T-WS₂ on the V₂O₃ film; scale bars: **(b)** up: 10 μm, down: 5 μm; **(c)** 1 nm, inset: 5 1/nm; **(d)** 0.5 nm; **(g)** 20 nm, inset: 1 nm; **(h)** 1 nm.

strongly dependent on the atomic weight. Figure 2d shows a magnified image of the region outlined by a white dashed rectangle in Fig. 2c. Both the STEM images display a hexagonal packing along [001] zone axis which is usually observed in monolayered 2H-WS₂ (Supplementary Fig. 4a), as highlighted by the fast Fourier transform (FFT, Fig. 2c inset), implying no 1T' reconstruction occurred^{1,18}. In particular, only W atoms are identified because of a much lower atomic number of S compared with W, and the invisible S atoms were also illustrated in the reported metallic WS₂ crystals^{1,16,22}. In addition to the invisible S atoms, the atomic positions where W atoms are replaced by V atoms can also be obscurely seen due to the significantly reduced contrast at the W atomic sites (marked by the white dashed circles). The electron energy-loss spectroscopy (EELS) of V SACs@1T-WS₂ in Fig. 2e shows two major features of V-L₂ (524.05 eV) and V-L₃ (517.03 eV) peaks assigned to V⁴⁺, affirming the V substitutions in the 1T-WS₂ layer³⁴. The EELS of S and O spectra in Supplementary Fig. 5 were shown to further reveal the presence of S and absence of O in the transferred 1T samples, excluding the V signals from V-based oxidations. The schematic atomic structure of V SACs@1T-WS₂ is depicted in Fig. 2d (right), in which we replace W atoms (blue spheres) of WS₂ with V atoms (red spheres) to illustrate isolated V atoms in 1T-WS₂. Moreover, the W-S-S intensity sequence in Fig. 2f (from the pink dashed arrow in Fig. 2d) is also indicative of the 1T phase of WS₂ due to a misaligned top and bottom S atom. In contrast, for the 2H-WS₂ in Supplementary Fig. 4b, the S atoms at the top and bottom sublayers are overlapped, leading to an alternating W and S intensity pattern. In addition,

W-S-S-V-S-S-W and W-V-W intensity profile sequences from both experimental and simulated STEM images are also achieved to verify the V atoms replacement at W sites (see details in Supplementary Figs. 6 and 7). It is anticipated that the V and S atoms could become visible if the 1T phase is transformed into the 2H phase, which has been shown in a pre-published literature³⁵. To further confirm the V-atom concentration in the 1T-WS₂ layer, we anneal the 1T-WS₂ sample at 200 °C (in the air for 30 min) for STEM imaging and find that the 1T phase is completely transformed into the 2H phase, as shown in Supplementary Figs. 8 and 9. Simultaneously, both the V atoms and S atoms are prominently discernible, in consistent with the STEM images of V-doped 2H-TMDs³⁵⁻³⁷. As a result, the substitutional V atoms are at an average concentration of 4.0 at% (~2.0 wt%) in the 1T-WS₂ layer. To exclude the presence of V-based contaminations (e.g., V₂O₃, VO₂, and VS₂) in the transferred 1T sample, XPS spectra of 1T sample transferred on highly oriented pyrolytic graphite were performed (see details in Supplementary Figs. 10-12). The V signal in Supplementary Figs. 11c and 12c were ascribed to the V-S bond³⁸, which was consistent with the EELS result in Fig. 2e.

The cross-sectional view STEM image of V SACs@1T-WS₂ on the sapphire substrate was carried out to confirm the epitaxial relationship between V₂O₃ and the sapphire substrate. Figure 2g shows a low-resolution STEM image, indicating a ~20 nm thickness of V₂O₃ film. The inset high-resolution STEM image displays a sharp interface between V₂O₃ and sapphire substrate, revealing the epitaxial growth of V₂O₃ film on the sapphire substrate³⁹. More importantly, we observe a single layer of WS₂

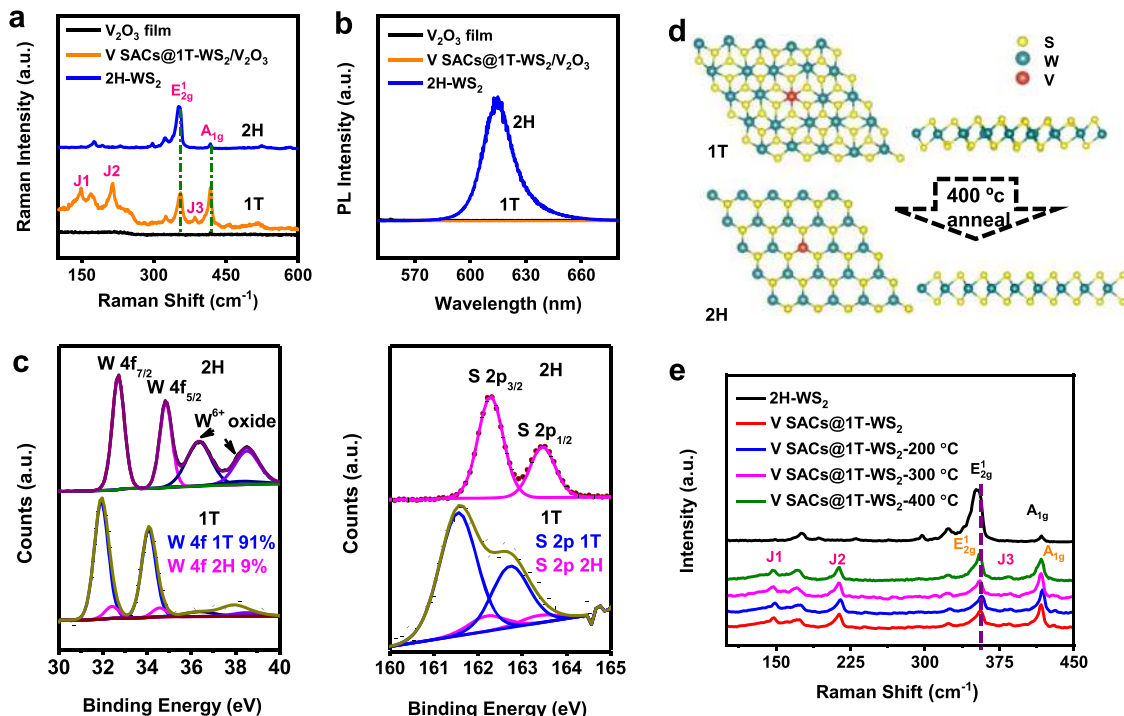


Fig. 3 Phase transition from 1T to 2H. **a** Raman spectra of V_2O_3 film (black), V SACs@1T- WS_2/V_2O_3 (orange), and 2H- WS_2 (blue). **b** PL spectra of V_2O_3 film (black), V SACs@1T- WS_2/V_2O_3 (orange), and 2H- WS_2 (blue). **c** High-resolution XPS spectra of W 4f (left) and S 2p (right) core level peak regions for 2H and 1T phase, respectively. The fitting blue and pink curves represent the contributions of 1T and 2H phases, respectively. **d** Schematic representation of the 1T to 2H structural phase transition occurring upon thermal annealing. **e** Raman spectra of 2H- WS_2 , V SACs@1T- WS_2 , and V SACs@1T- WS_2 with different annealing temperatures in H_2/Ar for 2 h.

from the sharp interface between V SACs@1T- WS_2 and V_2O_3 (Fig. 2h). The lattice spacing of V_2O_3 measured in the STEM image is ~ 0.23 nm, in correspondence with the (006) plane of V_2O_3 obtained from the XRD diffraction pattern in Supplementary Fig. 2³⁹. In addition, the monolayer thickness of V SACs@1T- WS_2 (before and after transferring) is also verified by atomic force microscope (AFM), as shown in Supplementary Fig. 13. Second-harmonic generation and angle-resolved-polarization Raman spectra (ARPRS) are commonly used to probe the symmetry and isotropic/anisotropic lattice structure of TMDs^{11,40,41}. Therefore, the high symmetry and isotropic nature of V SACs@1T- WS_2 have also been discussed in Supplementary Figs. 14 and 15.

Controlled phase conversion. The two different phases of 1T and 2H are easily highlighted by the confocal Raman spectroscopy, as provided in Fig. 3a, b. The Raman spectrum of V SACs@1T- WS_2 exhibits two prominent peaks at 418.4 cm^{-1} and 354.6 cm^{-1} (Fig. 3a, orange plot), corresponding to the A_{1g} and E_{2g}^1 resonance modes, respectively. Moreover, three additional typical peaks are observed at 147.9 cm^{-1} (J_1), 214.5 cm^{-1} (J_2), and 385.3 cm^{-1} (J_3), respectively, which only exist in the metallic phase but not in 2H- WS_2 monolayers (blue plot in Fig. 3a)^{1,16,18,22,42–45}. Particularly, a prominently merged peak in the range of $150\text{--}250\text{ cm}^{-1}$ can be ascribed to hexagonal V_2O_3 , as demonstrated in Supplementary Fig. 16. As verified in Supplementary Fig. 17, V_2O_3 film starts to nucleate when the temperature is elevated at $\sim 600^\circ\text{C}$. Hence, the different nucleation temperatures of V_2O_3 and WS_2 give rise to the sequential growth of V_2O_3 and WS_2 on the sapphire substrate. A brief discussion of the possible formation mechanism of the V_2O_3 film on the sapphire substrate is provided in Supplementary Fig. 17. In addition, we can see that the strongest photoluminescence (PL) signal (Fig. 3b, blue plot) is associated with

monolayered 2H- WS_2 ³¹, while the negligible PL signal (Fig. 3b and Supplementary Fig. 18, orange plot) from V@SACs@1T- WS_2 is presumably due to the metallic nature^{1,2}.

To illustrate the high purity of the obtained 1T phase, XPS spectra were performed to quantify the 1T and 2H compositions according to the high sensitivity of the tungsten signal to its oxidation state and coordination geometry^{1,46}. The V@SACs@1T- WS_2 monolayers were transferred on the fresh sapphire substrate for the XPS measurements. The survey scan of V@SACs@1T- WS_2 was shown in Supplementary Fig. 19a. The O 1s signal in Supplementary Fig. 19b was ascribed to sapphire substrate. As provided in Fig. 3c, the W 4f core level peak of 1T phase is shifted to lower binding energy of ~ 1.0 eV than that of 2H phase, assigning to a major amount as high as 91% of 1T phase. The decline in binding energy is presumably caused by the chemical reduction of W from +4 to the +3 oxidation state⁴⁷. The existence of 2H phase in the 1T sample may arise from the phase transition caused by the X-ray illumination, as no 2H characters have been detected from Raman spectra and STEM images, implying that a very high phase purity of the as-grown 1T sample (at least 91%). Notably, signals at higher binding energies of 36.3 eV and 38.5 eV from the 2H- WS_2 stand for the peaks of W $5p_{3/2}$ and W^{6+} oxidation state species, respectively. Simultaneously, the high-resolution of core level S 2p peaks is coherently manifested lower binding energy in contrast to the S 2p peak from the 2H phase, consistent with the previous XPS studies of metallic WS_2 ^{1,22}.

Moreover, the V SACs@1T- WS_2 monolayers are extremely stable under ambient conditions even after one year, as shown in Supplementary Fig. 20. Importantly, a high 1T phase ($\sim 60\%$) is preserved in the sample from the XPS analysis in Supplementary Fig. 21b, and the decrease of 1T/2H ratio should be probably caused by the oxidation of V_2O_3 film on the surface, as

demonstrated in Supplementary Fig. 21d. In addition, upon annealing at different temperatures (200 °C, 300 °C, and 400 °C, respectively) in H₂/Ar condition, the 1T phase is partially transformed into a 2H phase. The schematic structure of phase transition from 1T to 2H is shown in Fig. 3d. From the XPS spectra recorded in Supplementary Fig. 22, despite gradual shrinkage of W 4f and S 2p peaks from 1T phase with the elevated temperature ≥ 300 °C, a very high amount of 1T phase is still preserved even after annealing at 400 °C (~49%). The different ratios of 1T/2H (W 4f) under different annealing temperatures were summarized in Supplementary Table 2. Raman spectra in Fig. 3e reveal that the enhanced intensities of E_{2g}¹/A_{1g} are associated with the decreasing 1T phase. Remarkably, characteristic peaks assigned to the 1T phase are still observed after annealing at 400 °C. Interestingly, as the increasing temperature, the PL intensity in Supplementary Fig. 23 was enhanced and largely blue-shifted, which was ascribed to the variation of the band-structure caused by the pronounced ratio of 2H phase in the 1T sample, in consistent with the previously reported metallic TMDs²².

Growth mechanism of V SACs@1T-WS₂. Our fabrication of V SACs@1T-WS₂ monolayers by the one-step growth exemplifies the advantage of the CVD strategy over the exfoliated method

and wet-chemical method, where the phase purity cannot be well controlled (Supplementary Table 1). The octahedral 1T phase has long been considered as an energetically unfavorable structure and tends to be transformed into a more stable 1T' or 2H phase. Hence, understanding the growth mechanism of the present stable 1T structure is of importance for exploring more 1T-TMDs controllable growth. As demonstrated in Supplementary Fig. 17, the nucleation of V₂O₃ (at ~600 °C) precedes the epitaxial growth of WS₂ (~800 °C) during the whole growth. Stepwise-products experiments were designed to explore the origin of the V SACs@1T-WS₂ formation. The pristine one-step CVD growth was separated into two steps, that is initial V₂O₃ growth and subsequent V SACs@1T-WS₂ growth, as depicted in Fig. 4a.

In the first growth step, VCl₃ and sulfur were the co-precursors for the preparation of V₂O₃-nuclei film under the same growth condition with the pristine one-step growth. The presence of V₂O₃ was identified by the Raman spectrum in Supplementary Fig. 24a (blue plot) and XRD diffraction peaks in Supplementary Fig. 24b (blue plot). The oxygen element in the V₂O₃-nuclei film was presumably from the O₂ residue in the tube furnace, as V₂O₃-No nuclei film was also synthesized if using VCl₃ as the only precursor (Supplementary Fig. 24b, orange plot). Apart from the V₂O₃, trace amounts of VS₂ were also identified based on the XPS spectra analysis (Supplementary Fig. 24d, f). To further confirm the presence of VS₂, the V₂O₃-nuclei film was scraped

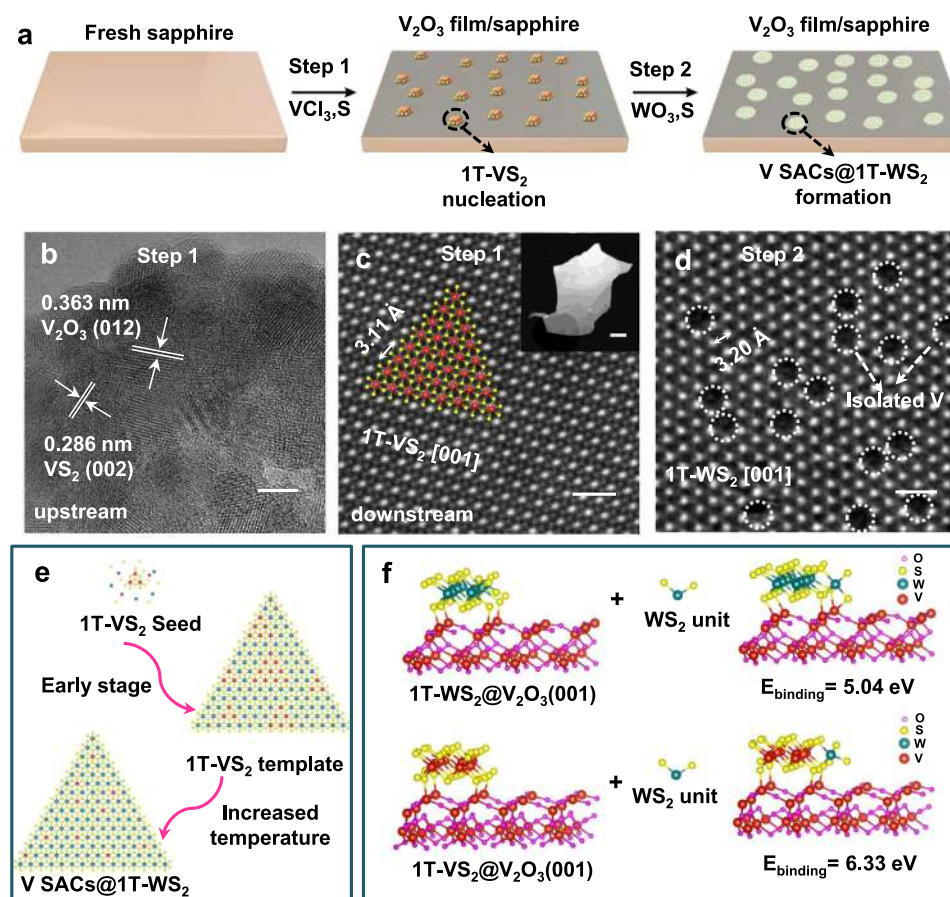


Fig. 4 Growth mechanism of V SACs@1T-WS₂. **a** Stepwise-products experiments for the V SACs@1T-WS₂ growth process. **b** HRTEM image of V₂O₃-nuclei film formed in the upstream of the sapphire substrate. **c** High-resolution HAADF-STEM image of 1T-VS₂ formed in the downstream of V₂O₃-nuclei film/sapphire substrate. The red spheres and yellow spheres represent the V atoms and S atoms, respectively, in the schematic model of 1T-VS₂ in the basal plane. Inset: low-resolution HAADF-STEM image of VS₂ domain. **d** High-resolution HAADF-STEM image of V SACs@1T-WS₂ formed on the surface of V₂O₃-nuclei film. The V atoms are highlighted by the dashed white circles. **e** The proposed growth mechanism of V SACs@1T-WS₂ formed on the V₂O₃ film. **f** Computed binding energy of WS₂ unit on 1T-WS₂ vs 1T-VS₂ on the surface of V₂O₃ (001). Scale bars: **(b)** 5 nm; **(c)** 0.5 nm, inset 50 nm; **(d)** 0.5 nm.

from the sapphire substrate for the HRTEM measurement, as shown in Fig. 4b. In addition to the lattice spacing of 0.363 nm from V_2O_3 , the other measured lattice spacing of ~ 0.286 nm can be well indexed with the (002) plane of 1T- VS_2 . Elemental mapping from the same region showed the uniform distributions of V, O, and S elements (Supplementary Fig. 25) in the V_2O_3 -nuclei film, which was coincident with the analysis of the XPS survey spectrum in Supplementary Fig. 24c. More interestingly, 1T- VS_2 nanocrystals were found on the surface of V_2O_3 -nuclei film further downstream (Supplementary Fig. 26b, c, lower growth temperature zone, $\sim 620^\circ\text{C}$). In contrast to the trace amounts of VS_2 nuclei found in the upstream (the hot center growth zone, $\sim 860^\circ\text{C}$), the VS_2 nanocrystals downstream can be easily transferred from the V_2O_3 -nuclei film using a standard transfer method for STEM imaging (Fig. 4c). The image showed a hexagonal atomic structure of 1T- VS_2 in the [001] basal plane⁴⁸, which was solid evidence that the VS_2 intermediates were nucleated on the surface of V_2O_3 during the growth.

In the second step, the as-produced V_2O_3 -nuclei film/sapphire substrate was put back into a fresh CVD process to collect the final product using WO_3 and sulfur as the co-precursors. Intriguingly, it was found that smaller 1T domains of WS_2 were formed on the surface of the film (Fig. 4d, Supplementary Fig. 27a, e), whereas 2H- WS_2 domains were achieved if using V_2O_3 -No nuclei film (Supplementary Fig. 27b, e, f) as the collecting substrate. Notably, nothing could be found if using commercial V_2O_3 (001) film (Supplementary Fig. 27c, d, and g), because that the rough surface and the low-quality of the commercial V_2O_3 were not in favor of the VS_2 and WS_2 nucleation on the surface. The 1T- or 2H- WS_2 domains were also confirmed by the Raman mapping in Supplementary Figs. 28 and 29. As a result, these experimental observations imply that both the VS_2 nucleation and the V_2O_3 film are very requisite for the V SACs@1T- WS_2 growth and VS_2 intermediates play the most important role in determining the 1T phase growth of WS_2 . The proposed growth mechanism is shown in Fig. 4e, in which the

1T- VS_2 nuclei formed in the early growth stage serve as the 1T structure template and significantly strengthen the binding of WS_2 unit (Fig. 4f, from 5.04 eV to 6.33 eV) on the V_2O_3 film, thereby triggering the epitaxial growth of the 1T phase nucleus. Such an epitaxially grown WS_2 layer should be the 1T phase instead of the 2H phase due to the much higher binding energy of 1T- VS_2 /1T- WS_2 (6.09 eV) than 1T- VS_2 /2H- WS_2 (4.19 eV) (Supplementary Fig. 30). The computed lattice parameters of 2H- WS_2 , V SACs@2H- WS_2 , and V SACs@1T- WS_2 are shown in Supplementary Table 3. In addition, it was also demonstrated that the amount of VCl_3 could significantly affect the controllable phase growth of WS_2 (see details in Supplementary Figs. 31–34). The influence of heating temperature on the synthesis of 1T- WS_2 has also been investigated, as displayed in Supplementary Figs. 35–37. Moreover, vanadocene precursors were also investigated to enrich the growth method of 1T- WS_2 monolayers (Supplementary Fig. 38).

HER activity of V SACs@1T- WS_2 . The as-produced V SACs@1T- WS_2 monolayers were transferred on the glass carbon (GC) electrode for the HER performance measurement using a three-electrode setup in 0.5 M H_2SO_4 . In addition, HER performance of the other investigated electrocatalysts, i.e., bare GC, 2H- WS_2 , 1T-400 (V SACs@1T- WS_2 annealed at 400°C in H_2/Ar for 2 h), 2H_{1T} (transformed by V SACs@1T- WS_2 annealed at 200°C in the air for 30 min) and commercial Pt/C-20 % were evaluated for comparison. As shown in linear sweep voltammetry (LSV) curves (Fig. 5a), V SACs@1T- WS_2 exhibited a low overpotential of 185 mV (η_{10}) at a current density of 10 mA/cm^2 with an ultralow mass loading of $1.8\text{--}6.5\text{ }\mu\text{g/cm}^2$ (see details in Supplementary Figs. S39–S45 and Supplementary Table 4–6), outperforming the 1T-400 (blue plot, $\eta_{10} = 325\text{ mV}$), 2H_{1T} (olive plot, $\eta_{10} = 515\text{ mV}$) and 2H (red plot, $\eta_{10} = 684\text{ mV}$) electrodes. The excellent activity of SACs@1T- WS_2 monolayers was further demonstrated by the comparisons of Tafel slopes for different catalysts, as shown in

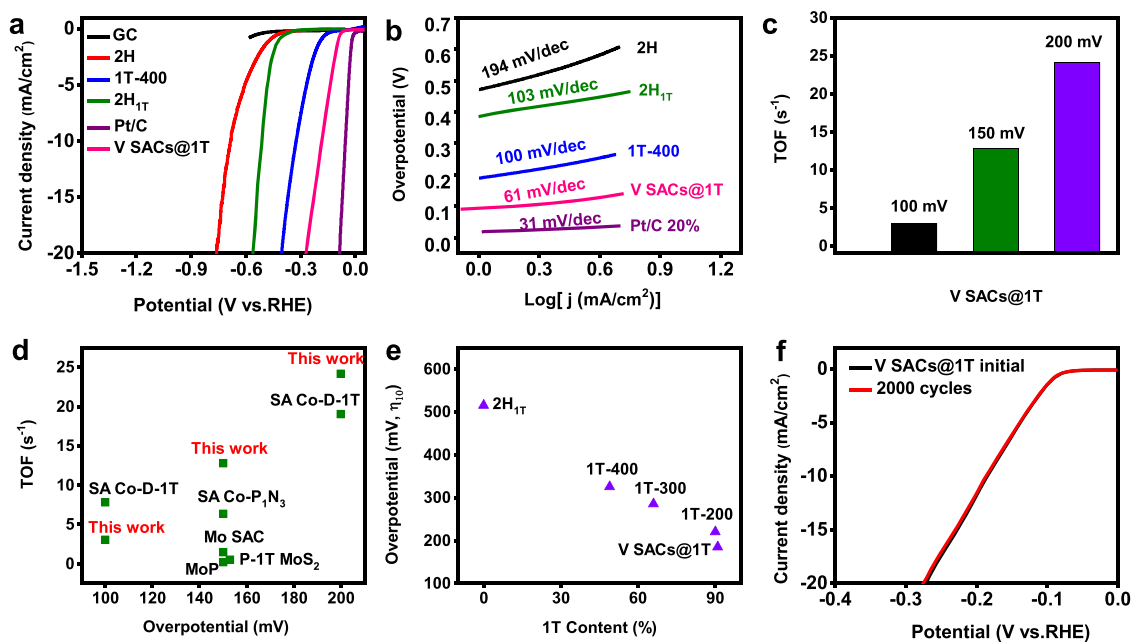


Fig. 5 HER performance of V SACs@1T- WS_2 . **a** LSV curves of GC, 2H (2H- WS_2), 1T-400 (V SACs@1T- WS_2 annealed at 400°C in H_2/Ar for 2 h), 2H_{1T} (V SACs@2H- WS_2 , transformed by V SACs@1T- WS_2), Pt/C (Pt/C 20%) and V SACs@1T- WS_2 electrodes in 0.5 M H_2SO_4 with a scan rate of 5 mV/s. **b** Tafel plots of 2H, 1T-400, 2H_{1T}, Pt/C 20% and V SACs@1T electrodes. **c** TOF values of V SACs@1T- WS_2 measured at different overpotentials. **d** TOF comparison with other representative electrocatalysts. **e** HER activity as a function of the 1T phase ratios obtained by annealing V SACs@1T- WS_2 in the H_2/Ar for 2 h. **f** Electrochemical stability of V SACs@1T- WS_2 after 2000 cycles of CV tests.

Fig. 5b. The Tafel slope for V SACs@1T-WS₂ was 61 mV/dec (Fig. 5c), which is much lower than that of 1T-400 (100 mV/dec), 2H_{1T} (103 mV/dec), and 2H-WS₂ (194 mV/dec). Please note that mass loading of electrocatalysts has a great impact on the measured activities; hence, it has generally used as catalyst performance metrics⁷. Although the mass loading of SACs@1T-WS₂ was much lower than most of the non-precious electrocatalysts (Supplementary Fig. 46), the HER performance was still comparable to that of strained 1T'-WS₂ nanosheets (NSs)¹, 1T'-MoS₂ NSs², 1T'-MoS₂ monolayers¹¹, and better than that of 2H-1T boundaries MoS₂ monolayers⁴⁹, 1T' WSe₂ NSs⁷ and PE-CVD 1T-WS₂ film¹⁵. The electrochemical surface area (ECSA) was calculated as an important factor to affect the catalytic activity of electrocatalysts^{50–52}. The calculated details were shown in the experimental section and Supplementary Fig. 47. Double-layer capacitance (C_{dl}) and ECSA values were 139.5 $\mu\text{F}/\text{cm}^2$ and 3.49 cm^2 for V SACs@1T-WS₂ and 61.7 $\mu\text{F}/\text{cm}^2$ and 1.54 cm^2 for 2H-WS₂, suggesting the critical contributions of V atom sites and high purity of 1T-WS₂. The TOF values of the SACs@1T-WS₂ (Fig. 5c) were obtained according to the precious reports^{23,53} and calculated to be 3.01 s^{-1} , 12.78 s^{-1} , and 24.15 s^{-1} at overpotentials of 100 mV, 150 mV, and 200 mV, respectively, which were much higher than those recently representative electrocatalysts listed in Fig. 5d and Supplementary Table 7.

As the V SACs@1T-WS₂ monolayers contain a high concentration of 1T phase, to investigate the influence of 1T content on the catalytic performance, the V SACs@1T-WS₂ electrode was gradually annealed at different temperatures and the HER activity after each annealing treatment was performed, ensuring that the identical dimensions and geometrical areas to evaluate the catalytic properties. Remarkably, the HER activities were strongly related to the 1T phase content as demonstrated by a gradual decrease in the η_{10} with decreasing 1T ratios (Fig. 5e). Remarkably, negligible activity degradation can be observed in the reproducible polarization curve of V SACs@1T-WS₂ in Fig. 5f even after 2000 continuous cycling, indicative of a good HER performance stability. The stability test was conducted at current densities higher than 10 mA/cm^2 in 0.5 M H₂SO₄ electrolyte for 100 h. As revealed by the chronoamperometric curve of V SACs 1T-WS₂ electrocatalyst in Supplementary Fig. 48, the current density for the V SACs 1T-WS₂ electrocatalyst displayed a slight current decay of 1.0 mA/cm^2 after 24 h and 3.4 mA/cm^2 after 100 h, indicating high stability of V SACs 1T-WS₂ catalyst. The metallic properties of V SACs 1T-WS₂ catalyst after stability test were also investigated by Raman spectroscopy (Supplementary

Fig. 49a), which showed obvious metallic peaks (J_1 , J_2 , J_3) in the Raman spectrum (red plot). Moreover, the STEM image showed in Supplementary Fig. 49b confirmed the V SACs 1T-WS₂ structure after the stability test. Both the Raman spectrum and STEM image indicated the robust 1T structure of V SACs 1T-WS₂ catalyst after HER test.

V SACs enhancing the HER activity of 1T-WS₂. Especially, the HER performance of 2H-WS₂, V SACs@2H-WS₂, and V SACs@1T-WS₂ was further studied using DFT considering both basal plane (Supplementary Fig. 50) and edge sites (Supplementary Figs. 51–53) as the active sites. Our calculations show that the V SACs could significantly influence the free energy of H adsorption (ΔG_H) on the edge sites of 1T-WS₂, as summarized in Supplementary Table 8. Please note that the $|\Delta G_H|$ of V SACs@1T-WS₂ at the basal plane is 0.4 eV, which is approximate to the $|\Delta G_H|$ of intrinsic 1T-WS₂ at 0.28 eV¹, implying that the single-atom V sites have a negligible influence on the HER performance of 1T-WS₂ in the basal plane. Compared to the 2H-WS₂ and V SACs@2H-WS₂, V SACs@1T-WS₂ exhibits the lowest $|\Delta G_H|$ (0.05 eV) at V-atom sites (Fig. 6a), indicating that the isolated V atoms are catalytically active in the layer of 1T-WS₂. The charge depletion at the active sites has been proven to play an essential role in improving the electrochemical activity of the catalysts^{13,54}. To acquire a deeper understanding of how single V atoms enhanced the activity of 1T-WS₂, the charge redistribution of V SACs@1T-WS₂ was studied. As shown in the inset image in Fig. 6b, we can clearly see that when one W atom was substituted by a V atom, there was more charge depletion generated at the V-atom site. Such variations in the local electronic structure can also be well described using the d-band theory⁵⁵. A linear inverse correlation between $|\Delta G_H|$ and the d-band center at the most active edge sites were revealed, indicating that a more negative d-band center corresponds to more occupation of the antibonding states, resulting in weaker H adsorption of V SACs@1T-WS₂ comparable to their 2H counterparts.

Discussion

In summary, we have demonstrated a direct synthesis of single-atom V sites on the high purity 1T-WS₂ monolayers via a one-step CVD strategy through introducing VCl₃ as a co-precursor, with much better HER performance than the 2H counterparts. The step-wise experimental findings together with DFT results shed light on the understanding of the CVD-grown V SACs@1T-WS₂ monolayers, that is the 1T-WS₂ nuclei initially act as the 1T template structures for

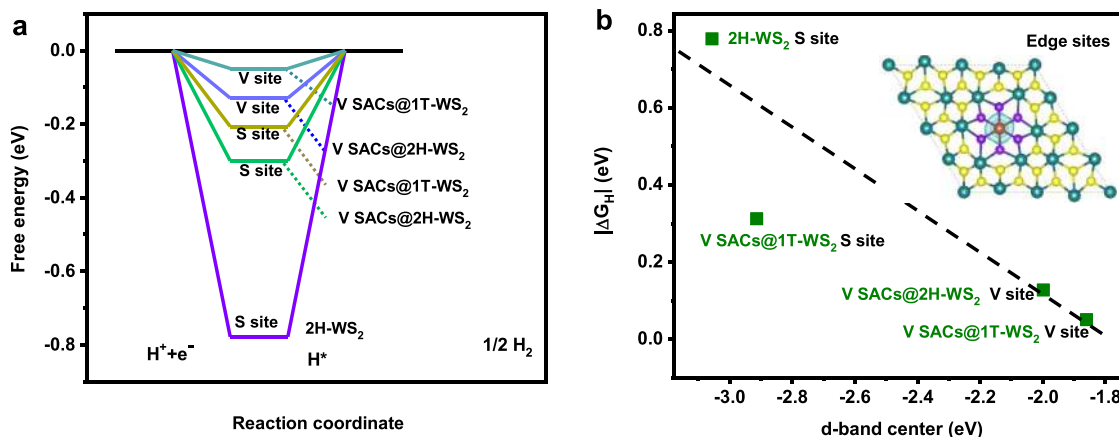


Fig. 6 HER activity mechanism of V SACs@1T-WS₂. **a** The Gibbs free energy of H adsorption (ΔG_H) of 2H-WS₂, V SACs@2H-WS₂, and V SACs@1T-WS₂ on the V and S edge sites. **b** Relationship between $|\Delta G_H|$ and the d-band center of adjacent W/V ions at the most active edge sites of 2H-WS₂, V SACs@2H-WS₂, and V SACs@1T-WS₂.

the follow-up V SACs@1T-WS₂ growth on the V₂O₃ film. The HER performance of intrinsic 1T-WS₂ was remarkably boosted after the modification of isolated V atoms. DFT calculations highlight that the highly activated V-atom sites primarily account for the excellent HER activity of V SACs@1T-WS₂ monolayers. Our findings could fill the gap of SACs grown via a one-step CVD strategy and pave the way to design more efficient and robust electrocatalysts for applications in water splitting.

Methods

The growth of V SACs@1T-WS₂ monolayers, 2H-WS₂ monolayers, V₂O₃ film.

In the growth of monolayer V SACs@1T-WS₂, sulfur (Sigma-Aldrich, 99%), tungsten trioxide (WO₃, Sigma-Aldrich, 99.99%), and vanadium (III) chloride (VCl₃, Sigma-Aldrich, 99%) were used as the growth precursors. Two quartz boats with 0.03 g of VCl₃ powder (in the hot center) and 0.30 g WO₃ powder (the upstream of VCl₃) were placed sequentially in the hot center of the furnace. And a fresh sapphire (c-plane) substrate (1 cm × 2 cm) was placed face-down of the quartz boat to collect the final product. The heating temperature was kept at 860 °C. The S powder was placed in a separate quartz boat at the upper stream side of the cold zone and the temperature was maintained at 160 °C during the reaction. The gas flow has consisted of an ultrapure mixed Ar/H₂ (Ar = 80 sccm, H₂ = 20 sccm), and the chamber pressure was controlled at 10 Torr. After reaching the desired growth temperature of 860 °C, the heating zone was kept for 15 min and the furnace was then naturally cooled down to room temperature. The V₂O₃ film was simultaneously formed during the V SACs@1T-WS₂ growth. The commercial V₂O₃ (001) film on the c-plane sapphire was purchased from Xi'an Qiyue Biotechnology Co., Ltd. To obtain 2H-WS₂ monolayers, we used WO₃ and sulfur as the precursors with the same growth condition with V SACs@1T-WS₂. To obtain V₂O₃-No nuclei film, we used the only VCl₃ as the precursors with the same growth condition. To obtain V₂O₃-nuclei film, we used only VCl₃ and sulfur as the precursors with the same growth condition.

V₂O₃ film growth mechanism and characterization. According to the lattice parameters of V₂O₃ and sapphire (V₂O₃: hexagonal, *a* = 0.492 nm, *c* = 1.397 nm; α-Al₂O₃: hexagonal, *a* = 0.475 nm, *c* = 1.297 nm), hexagonal V₂O₃ shares the same lattice-type and similar lattice parameters with α-Al₂O₃; thus, it is expected to epitaxially grow on α-Al₂O₃ with the relationship V₂O₃ (001)||001//α-Al₂O₃ (001)||100^{39,56–58}.

To investigate the growth mechanism of V₂O₃ film, we prepared V₂O₃-No nuclei film under different temperatures, as exhibited in Supplementary Fig. 17a. It can be observed that V₂O₃ film could be formed at ≥600 °C during the temperature-dependent controllable experiments. Particularly, a merged peak in the range of 150–250 cm⁻¹ was observed in the Raman spectrum and the peak was correlated to both monoclinic A_{1g} and hexagonal V₂O₃ A_{1g} symmetry, indicative of a mixed phase. However, the additional peaks of low intensity at 300 cm⁻¹ and 500 cm⁻¹ were solely attributable to hexagonal V₂O₃^{59,60}, indicating the hexagonal structure of the as-grown V₂O₃ film. Under the temperature of 600 °C, low-quality film or nothing will be formed on the sapphire substrate. Simultaneously, we measured the Raman spectra of the powders from the VCl₃ quartz boat after each growth reaction with different growth temperatures, as shown in Supplementary Fig. 17b. VO₂ (B) will be evidently formed after the decomposition of VCl₃⁶¹ (see Eqs. (1) and (2) in Supplementary Fig. 17).

Transfer process of V SACs@1T-WS₂, 2H-WS₂, V₂O₃-nuclei film. The as-grown samples were transferred onto arbitrary substrates, such as fresh sapphire, SiO₂/Si, GC, and holy-carbon nickel TEM Grid using a modified method in our lab. First, poly (methyl methacrylate) (PMMA) was spin-coated onto the samples followed by 120 °C baking for 10 min, and then etched by 5% HF solution for 2–3 min. The PMMA/sample was gently peeled off by the tweezers and deposited onto the targeted substrates. PMMA/sample/targeted substrate was baked for 1 h at 120 °C in air. The PMMA was removed by acetone and cleaned with isopropyl alcohol. The V₂O₃-nuclei film was scratched by tweezers and ultrasonic the V₂O₃/sapphire sample in the ethanol solution for 15 min for the HRTEM measurement. The sample was prepared by dropping the solution onto the holy-carbon nickel TEM grid.

For the STEM measurements samples, the extra annealing process was necessary to remove the residual PMMA. For the 2H-WS₂ sample annealing, the sample was located in a vacuum container (less than 10⁻⁶ Torr) at 350 °C overnight. For the V SACs@1T-WS₂ sample annealing, the sample was located in a vacuum container (less than 10⁻⁶ Torr) at 200 °C for 2 h. For the XPS and Raman spectra of V SACs@1T-WS₂ annealed at different temperatures, the V SACs@1T-WS₂ monolayers were transferred on the fresh sapphire substrates and annealed in H₂/Ar condition with different temperatures.

Characterization. Optical spectroscopy is collected under a Witec alpha 300 R confocal Raman microscopic system. Gratings of 1800 lg/mm and 300 lg/mm are selected for the high-resolution Raman spectrum and wide range PL spectrum, respectively. The TMDs are excited by 532 nm laser with a power of 1 mW and

spot size of 0.5 μm and emitted Raman signal is collected by 100× objective (N.A = 0.9) from a Carl Zeiss Microscopy. ARPRS are conducted on a triple-grating micro-Raman spectrometer (Horiba-JY T64000) with a 532 nm laser under a backscattering configuration. The polarization is resolved by rotating sample orientation on the normal axis of the basal plane. The emitted Raman signal is collected through a 100× objective, dispersed with 1800 lg/mm grating, and detected by a charge-coupled device.

An AFM (Cypher ES environmental AFM) was utilized to obtain the morphology images and the height profile of V SACs@WS₂ monolayers. The crystalline of the different samples was probed using a Bruker D8 advance powder XRD with Cu Kα radiation. X-ray photoelectron spectroscopy (XPS) studies were carried out in a Kratos Axis Ultra DLD spectrometer equipped with a monochromatic Al Kα X-ray source (*hν* = 1486.6 eV) under a vacuum of 1 × 10⁻⁹ mbar. The spectra were collected at fixed analyzer pass energies of 160 eV and 20 eV. The binding energies in XPS analysis were corrected by referencing C 1s line at 284.8 eV. STEM and TEM images were performed by Titan 40-300 Themis Z TEM from Thermo Fisher, USA (former FEI Co) equipped with a double Cs corrector, an electron monochromator, and a Gatan imaging filter quantum 966. The microscope was operated at 80 kV to minimize electron beam induced. Probe semi convergence angle was tuned to 30 mrad and probe current to 50 pA. For high-angle annular dark-field (HAADF) STEM images the inner collection angle was about 80 mrad. Radial Wiener filter was carried out to enhance the visibility of atoms

Computational details. First-principles simulations were performed at the DFT level implemented by the Vienna ab initio simulation package^{62–65} with the all-electron projector augmented wave model⁶⁶ and Perdew–Burke–Ernzerhof functions⁶⁷. The DFT-D₃ method was applied to include vdW interaction corrections⁶⁸. A kinetic energy cutoff of 400 eV was used for the plane-wave expansion of the electronic wave function. The convergence criteria of force and energy were set as 0.01 eV Å⁻¹ and 10⁻⁵ eV, respectively. Gaussian smearing of 0.1 eV was applied for optimization. A k-point grid with a 4 × 4 × 1 gamma-centered mesh was used for the WS₂ unit cell. For supercells that contain a larger number of vanadium and oxygen atoms, a corresponding number of k-points were used to keep the k-mesh spacing constant across different structures. The climbing image nudged elastic band was applied for transition state optimization⁶⁹.

The free energy of the adsorption atomic hydrogen (ΔG_H) is obtained by $\Delta G_H = \Delta E_H + \Delta E_{ZPE} - T\Delta S_H$. ΔE_H is the adsorption energy defined by $\Delta E_H = E_{sur} - H - E_{sur} + \frac{1}{2} E_{H_2}$. According to previous reports, ΔG_H can be written as $\Delta G_H = \Delta E_H + 0.25$, where 0.25 eV is the contribution from ZPE and entropy at 298 K⁷⁰.

Electrochemical measurements. Electrochemical measurements were carried in a PGSTAT 302N Autolab Potentiostat/Galvanostat (Metrohm) at room temperature. Graphite rod and Ag/AgCl (in a saturated KCl solution) electrodes were employed as the counter and reference electrodes, respectively. The V SACs@1T-WS₂ and 2H-WS₂ were transferred onto the GC electrodes as the working electrodes and dried. Nafion solution (0.5%) was drop-cast to protect WS₂ film. The V SACs@1T-400 electrode was prepared by annealing the V SACs@1T-WS₂ electrode at 400 °C in H₂/Ar for 2 h. The 2H_{1T} electrode was prepared by annealing the V SACs@1T-WS₂ electrode at 200 °C in the air for 30 min. The HER activities of different samples were evaluated by measuring polarization curves with LSV at a scan rate of 0.5 mV/s in 0.5 M H₂SO₄ solutions. Potentials were referenced to a reversible hydrogen electrode (RHE). The commercial Pt/C (20 wt% Pt on Vulcan carbon black) supported by GC was prepared by mixing the Pt/C, nafion, and isopropanol, sonicating for 30 min, and drop-casting on the GC. The mass loading of Pt/C was 500 μg/cm². The potential cycling was performed between 0.197 and -0.6 V vs RHE at 5 mV s⁻¹. All data have been corrected for a small ohmic drop based on impedance spectroscopy. ECSA and *C_{dl}* are determined by cyclic voltammograms at various scan rates (10, 30, 50, 70, 90, 110, 130, 150, 170, 190, and 210 mV/s) in the potential range (0.15–0.35 V vs. RHE). The capacitive currents (Δj) are plotted as a function of scan rate and *C_{dl}* is equal to half of the slope. The reference specific capacitance (*C_s*) of 40 μF/cm² is used in this work. The ECSA for the different catalysts are achieved based on the following equation

$$ECSA = \frac{C_{dl}}{C_s}$$

Calculation of turnover frequency. The TOF calculation details were specified as below, which was reported elsewhere^{23,53}.

$$TOF = \frac{\text{Total hydrogen turnovers per geometric area}}{\text{active sites per geometric area}}$$

The total hydrogen turnovers were calculated from the current density in the LSV polarization curve according to the equation as below:

$$\text{Total hydrogen turnovers} = \left(j \frac{\text{mA}}{\text{cm}^2} \right) \left(\frac{1 \text{C/s}}{1000 \text{ mA}} \right) \left(\frac{1 \text{mol e}^-}{96485 \text{ C}} \right) \left(\frac{1 \text{mol}}{2 \text{mol e}^-} \right) \left(\frac{6.022 \times 10^{23} \text{molecules H}_2}{1 \text{mol H}_2} \right)$$

The number of active sites in the V SACs@1T-WS₂ catalyst was obtained from the mass loading on the glass carbon electrode.

$$\text{Active sites} = \left(\frac{\text{electrocatalyst loading per geometric area} \left(\frac{\mu\text{g}}{\text{cm}^2} \right) \times \text{Vwt}\%}{VM_w \left(\frac{\mu\text{mol}}{\text{mol}} \right)} \right) \left(\frac{6.022 \times 10^{23} \text{ V atoms}}{1 \text{ mol V}} \right)$$

Data availability

The data that support the findings of this study are available from the corresponding author upon request.

Received: 25 May 2020; Accepted: 5 January 2021;

Published online: 29 January 2021

References

- Voiry, D. et al. Enhanced catalytic activity in strained chemically exfoliated WS₂ nanosheets for hydrogen evolution. *Nat. Mater.* **12**, 850–855 (2013).
- Yu, Y. et al. High phase-purity 1T'-MoS₂- and 1T'-MoSe₂-layered crystals. *Nat. Chem.* **10**, 638–643 (2018).
- Liao, G. et al. Semiconductor polymeric graphitic carbon nitride photocatalysts: the “holy grail” for the photocatalytic hydrogen evolution reaction under visible light. *Energy Environ. Sci.* **12**, 2080–2147 (2019).
- Liao, G. et al. Ag-based nanocomposites: synthesis and applications in catalysis. *Nanoscale* **11**, 7062–7096 (2019).
- Thalluri, S. M. et al. Inverted pyramid textured p-silicon covered with Co₂P as an efficient and stable solar hydrogen evolution photocathode. *ACS Energy Lett.* **4**, 1755–1762 (2019).
- Chen, X. et al. High phase-purity 1T-MoS₂ ultrathin nanosheets by a spatially confined template. *Angew. Chem. Int. Ed.* **58**, 17621 (2019).
- Sokolikova, M. S., Sherrell, P. C., Palczynski, P., Bemmer, V. L. & Mattevi, C. Direct solution-phase synthesis of 1T' WSe₂ nanosheets. *Nat. Commun.* **10**, 712 (2019).
- Kuznetsov, D. A. et al. Single site cobalt substitution in 2D molybdenum carbide (MXene) enhances catalytic activity in the hydrogen evolution reaction. *J. Am. Chem. Soc.* **141**, 17809–17816 (2019).
- Fu, W. et al. Epitaxial growth of graphene on V₈C₇ nanomeshes for highly efficient and stable hydrogen evolution reaction. *J. Catal.* **369**, 47–53 (2019).
- Jaramillo, T. F. et al. Identification of active edge sites for electrochemical H₂ evolution from MoS₂ nanocatalysts. *Science* **317**, 100–102 (2007).
- Liu, L. et al. Phase-selective synthesis of 1T' MoS₂ monolayers and heterophase bilayers. *Nat. Mater.* **17**, 1108–1114 (2018).
- Duerloo, K.-A. N., Li, Y. & Reed, E. J. Structural phase transitions in two-dimensional Mo- and W-dichalcogenide monolayers. *Nat. Commun.* **5**, 4214 (2014).
- Deng, S. et al. Synergistic doping and intercalation: realizing deep phase modulation on MoS₂ arrays for high-efficiency hydrogen evolution reaction. *Angew. Chem. Int. Ed.* **58**, 16289–16296 (2019).
- Enyashin, A. N. et al. New route for stabilization of 1T-WS₂ and MoS₂ phases. *J. Phys. Chem. C* **115**, 24586–24591 (2011).
- Kim, H.-U. et al. Wafer-scale and low-temperature growth of 1T-WS₂ film for efficient and stable hydrogen evolution reaction. *Small* **16**, 1905000 (2020).
- Liu, Q. et al. Stable metallic 1T-WS₂ nanoribbons intercalated with ammonia ions: the correlation between structure and electrical/optical properties. *Adv. Mater.* **27**, 4837–4844 (2015).
- Lukowski, M. A. et al. Enhanced hydrogen evolution catalysis from chemically exfoliated metallic MoS₂ nanosheets. *J. Am. Chem. Soc.* **135**, 10274–10277 (2013).
- Mahler, B., Hoepfner, V., Liao, K. & Ozin, G. A. Colloidal synthesis of 1T-WS₂ and 2H-WS₂ nanosheets: applications for photocatalytic hydrogen evolution. *J. Am. Chem. Soc.* **136**, 14121–14127 (2014).
- Park, J. C. et al. Phase-engineered synthesis of centimeter-scale 1T' and 2H-molybdenum ditelluride thin films. *ACS Nano* **9**, 6548–6554 (2015).
- Voiry, D. et al. Conducting MoS₂ nanosheets as catalysts for hydrogen evolution reaction. *Nano Lett.* **13**, 6222–6227 (2013).
- Yin, Y. et al. Contributions of phase, sulfur vacancies, and edges to the hydrogen evolution reaction catalytic activity of porous molybdenum disulfide nanosheets. *J. Am. Chem. Soc.* **138**, 7965–7972 (2016).
- Zhao, X., Ma, X., Sun, J., Li, D. & Yang, X. Enhanced catalytic activities of surfactant-assisted exfoliated WS₂ nanodots for hydrogen evolution. *ACS Nano* **10**, 2159–2166 (2016).
- Qi, K. et al. Single-atom cobalt array bound to distorted 1T MoS₂ with ensemble effect for hydrogen evolution catalysis. *Nat. Commun.* **10**, 5231 (2019).
- Zhang, H., Yu, L., Chen, T., Zhou, W. & Lou, X. W. Surface modulation of hierarchical MoS₂ nanosheets by Ni single atoms for enhanced electrocatalytic hydrogen evolution. *Adv. Funct. Mater.* **28**, 1807086 (2018).
- Deng, J. et al. Triggering the electrocatalytic hydrogen evolution activity of the inert two-dimensional MoS₂ surface via single-atom metal doping. *Energy Environ. Sci.* **8**, 1594–1601 (2015).
- Chow, P. K. et al. Wetting of mono and few-layered WS₂ and MoS₂ films supported on Si/SiO₂ substrates. *ACS Nano* **9**, 3023–3031 (2015).
- Elias, A. L. et al. Controlled synthesis and transfer of large-area WS₂ sheets: from single layer to few layers. *ACS Nano* **7**, 5235–5242 (2013).
- Gutiérrez, H. R. et al. Extraordinary room-temperature photoluminescence in triangular WS₂ monolayers. *Nano Lett.* **13**, 3447–3454 (2013).
- Perea-López, N. et al. Photosensor device based on few-layered WS₂ films. *Adv. Funct. Mater.* **23**, 5511–5517 (2013).
- Cui, Y. et al. High-performance monolayer WS₂ field-effect transistors on high-k dielectrics. *Adv. Mater.* **27**, 5230–5234 (2015).
- Gao, Y. et al. Large-area synthesis of high-quality and uniform monolayer WS₂ on reusable Au foils. *Nat. Commun.* **6**, 8569 (2015).
- Yang, W. et al. Electrically tunable valley-light emitting diode (vLED) based on CVD-grown monolayer WS₂. *Nano Lett.* **16**, 1560–1567 (2016).
- Jeong, H. Y. et al. Heterogeneous defect domains in single-crystalline hexagonal WS₂. *Adv. Mater.* **29**, 1605043 (2017).
- Laffont, L. et al. High resolution EELS of Cu–V oxides: application to batteries materials. *Micron* **37**, 459–464 (2006).
- Zhang, F. et al. Monolayer vanadium-doped tungsten disulfide: a room-temperature dilute magnetic semiconductor. *Adv. Sci.* **7**, 2001174 (2020).
- Pham, Y. T. H. et al. Tunable ferromagnetism and thermally induced spin flip in vanadium-doped tungsten diselenide monolayers at room temperature. *Adv. Mater.* **32**, 2003607 (2020).
- Yun, S. J. et al. Ferromagnetic order at room temperature in monolayer WSe₂ semiconductor via vanadium dopant. *Adv. Sci.* **7**, 1903076 (2020).
- Yu, S. H. et al. In situ hybridizing MoS₂ microflowers on VS₂ microflakes in a one-pot CVD process for electrolytic hydrogen evolution reaction. *ACS Appl. Energy Mater.* **2**, 5799–5808 (2019).
- Sun, G., Cao, X., Long, S., Li, R. & Jin, P. Optical and electrical performance of the thermochromic V₂O₃ thin film fabricated by magnetron sputtering. *Appl. Phys. Lett.* **111**, 053901 (2017).
- Beams, R. et al. Characterization of few-layer 1T' MoTe₂ by polarization-resolved second harmonic generation and Raman scattering. *ACS Nano* **10**, 9626–9636 (2016).
- Wang, Y. et al. Structural phase transition in monolayer MoTe₂ driven by electrostatic doping. *Nature* **550**, 487 (2017).
- Loh, T. A. & Chua, D. H. Origin of hybrid 1T- and 2H-WS₂ ultrathin layers by pulsed laser deposition. *J. Phys. Chem.* **119**, 27496–27504 (2015).
- Loh, T. A. J., Chua, D. H. C. & Wee, A. T. S. One-step synthesis of few-layer WS₂ by pulsed laser deposition. *Sci. Rep.* **5**, 18116 (2015).
- Tan, S. J. et al. Chemical stabilization of 1T' phase transition metal dichalcogenides with giant optical Kerr nonlinearity. *J. Am. Chem. Soc.* **139**, 2504–2511 (2017).
- Tsai, H.-L., Heising, J., Schindler, J. L., Kannewurf, C. R. & Kanatzidis, M. G. Exfoliated–restacked phase of WS₂. *Chem. Mater.* **9**, 879–882 (1997).
- Chen, W. et al. Quantum dots of 1T phase transitional metal dichalcogenides generated via electrochemical Li intercalation. *ACS Nano* **12**, 308–316 (2018).
- Kappera, R. et al. Phase-engineered low-resistance contacts for ultrathin MoS₂ transistors. *Nat. Mater.* **13**, 1128 (2014).
- Yuan, J. et al. Facile synthesis of single crystal vanadium disulfide nanosheets by chemical vapor deposition for efficient hydrogen evolution reaction. *Adv. Mater.* **27**, 5605–5609 (2015).
- Zhu, J. et al. Boundary activated hydrogen evolution reaction on monolayer MoS₂. *Nat. Commun.* **10**, 1348 (2019).
- Anjum, M. A. R., Jeong, H. Y., Lee, M. H., Shin, H. S. & Lee, J. S. Efficient hydrogen evolution reaction catalysis in alkaline media by all-in-one MoS₂ with multifunctional active sites. *Adv. Mater.* **30**, 1707105 (2018).
- McCrory, C. C. L. et al. Benchmarking hydrogen evolving reaction and oxygen evolving reaction electrocatalysts for solar water splitting devices. *J. Am. Chem. Soc.* **137**, 4347–4357 (2015).
- Voiry, D. et al. Best practices for reporting electrocatalytic performance of nanomaterials. *ACS Nano* **12**, 9635–9638 (2018).
- Wan, J. et al. In situ phosphatizing of triphenylphosphine encapsulated within metal–organic frameworks to design atomic Co₁-P₁N₃ interfacial structure for promoting catalytic performance. *J. Am. Chem. Soc.* **142**, 8431–8439 (2020).
- Zhao, Z., Li, M., Zhang, L., Dai, L. & Xia, Z. Design principles for heteroatom-doped carbon nanomaterials as highly efficient catalysts for fuel cells and metal-air batteries. *Adv. Mater.* **27**, 6834–6840 (2015).
- Chen, H. et al. Promoting subordinate, efficient ruthenium sites with interstitial silicon for Pt-Like electrocatalytic activity. *Angew. Chem. Int. Ed.* **58**, 11409–11413 (2019).
- Ji, Y. D. et al. Epitaxial growth and metal-insulator transition of vanadium oxide thin films with controllable phases. *Appl. Phys. Lett.* **101**, 071902 (2012).
- Allimi, B. S. et al. Growth of V₂O₃ thin films on a-plane (110) and c-plane (001) sapphire via pulsed-laser deposition. *J. Mater. Res.* **22**, 2825–2831 (2007).

58. Sakai, J., Limelette, P. & Funakubo, H. Transport properties and c/a ratio of V_2O_3 thin films grown on C- and R- plane sapphire substrates by pulsed laser deposition. *Appl. Phys. Lett.* **107**, 241901 (2015).
59. Kafizas, A., Hyett, G. & Parkin, I. P. Combinatorial atmospheric pressure chemical vapour deposition (cAPCVD) of a mixed vanadium oxide and vanadium oxynitride thin film. *J. Mater. Chem.* **19**, 1399–1408 (2009).
60. Kuroda, N. & Fan, H. Y. Raman scattering and phase transitions of V_2O_3 . *Phys. Rev. B* **16**, 5003–5008 (1977).
61. Xu, H. F., Liu, Y., Wei, N. & Jin, S. W. From $VO_2(B)$ to $VO_2(A)$ nanorods: hydrothermal synthesis, evolution and optical properties in $V_2O_5H_2C_2O_4H_2O$ system. *Optik* **125**, 6078–6081 (2014).
62. Kresse, G. & Furthmüller, J. Efficiency of ab-initio total energy calculations for metals and semiconductors using a plane-wave basis set. *Comput. Mater. Sci.* **6**, 15–50 (1996).
63. Kresse, G. & Furthmüller, J. Efficient iterative schemes for ab initio total-energy calculations using a plane-wave basis set. *Phys. Rev. B* **54**, 11169–11186 (1996).
64. Kresse, G. & Hafner, J. Ab initio molecular dynamics for liquid metals. *Phys. Rev. B* **47**, 558–561 (1993).
65. Kresse, G. & Hafner, J. Ab initio molecular-dynamics simulation of the liquid-metal–amorphous-semiconductor transition in germanium. *Phys. Rev. B* **49**, 14251–14269 (1994).
66. Blöchl, P. E. Projector augmented-wave method. *Phys. Rev. B* **50**, 17953–17979 (1994).
67. Perdew, J. P., Burke, K. & Ernzerhof, M. Generalized gradient approximation made simple. *Phys. Rev. B* **77**, 3865–3868 (1996).
68. Grimme, S., Antony, J., Ehrlich, S. & Krieg, H. A consistent and accurate ab initio parametrization of density functional dispersion correction (DFT-D) for the 94 elements H–Pu. *J. Chem. Phys.* **132**, 154104 (2010).
69. Henkelman, G., Uberuaga, B. P. & Jónsson, H. A climbing image nudged elastic band method for finding saddle points and minimum energy paths. *J. Chem. Phys.* **113**, 9901–9904 (2000).
70. Tang, Q. & Jiang, D.-E. Mechanism of hydrogen evolution reaction on 1T-MoS₂ from first principles. *ACS Catal.* **6**, 4953–4961 (2016).

Acknowledgements

L.L. acknowledges support from King Abdullah University of Science and Technology (Saudi Arabia). Y.L. and D.W. acknowledge support from the National Key R&D Program of China (2018YFA0702003) and the National Natural Science Foundation of China (21890383, 21671117, 21871159). W.Z. acknowledges support from the Educational Commission of Guangdong Province project (No.2015KJGJHZ006).

Author contributions

Y.L., L.L., and D.W. conceived the idea and designed the research project. A.H. designed the synthesis and performance experiments, collected and analyzed the data, and wrote the manuscript. X.Z. contributed to the characterizations of samples and wrote the manuscript. X.W. contributed to the computational results and wrote the manuscript. S.L. designed the optical characterizations experiments, analyzed the data, and wrote the manuscript. L.G. and Q.Z. designed the simulation STEM analyzes. Q.X., Z.Z., F.L., W.Z. contributed to revising the manuscript. All the authors commented on the manuscript and have given approval to the final version of the manuscript.

Competing interests

The authors declare no competing interests.

Additional information

Supplementary information is available for this paper at <https://doi.org/10.1038/s41467-021-20951-9>.

Correspondence and requests for materials should be addressed to D.W. or L.-J.L.

Peer review information *Nature Communications* thanks Baizeng Fang, Shaojun Guo, and other, anonymous reviewers for their contributions to the peer review of this work. Peer review reports are available.

Reprints and permission information is available at <http://www.nature.com/reprints>

Publisher's note Springer Nature remains neutral with regard to jurisdictional claims in published maps and institutional affiliations.



Open Access This article is licensed under a Creative Commons Attribution 4.0 International License, which permits use, sharing, adaptation, distribution and reproduction in any medium or format, as long as you give appropriate credit to the original author(s) and the source, provide a link to the Creative Commons license, and indicate if changes were made. The images or other third party material in this article are included in the article's Creative Commons license, unless indicated otherwise in a credit line to the material. If material is not included in the article's Creative Commons license and your intended use is not permitted by statutory regulation or exceeds the permitted use, you will need to obtain permission directly from the copyright holder. To view a copy of this license, visit <http://creativecommons.org/licenses/by/4.0/>.

© The Author(s) 2021